The Astronomical Journal, 168:273 (14pp), 2024 December https://doi.org/10.3847/1538-3881/ad7fe8

Searching for GEMS: TOI-6383Ab, a Giant Planet Transiting an M3-dwarf Star in a Binary System*

Lia Marta Bernabò[1,2], Shubham Kanodia[3], Caleb I. Cañas[4], William D. Cochran[2,5], Szilárd Csizmadia[1,6], Suvrath Mahadevan[7,8,9], Gudhmundur Stefánsson[10], Arvind F. Gupta[11], Andrew Monson[12], Henry A. Kobulnicky[13], Alexander K. Larsen[13], Ethan G. Cotter[13], Alexina Birkholz[13], Tera N. Swaby[13], Gregory Zeimann[14], Chad F. Bender[12], Scott A. Diddams[15,16], Jessica E. Libby-Roberts[7,8], Andrea S. J. Lin[7,8], Joe P. Ninan[17], Heike Rauer[1,18], Varghese Reji[17], Paul Robertson[19], Arpita Roy[20], and Christian Schwab[21]

[1] Institute of Planetary Research, German Aerospace Center (DLR), Rutherfordstrasse 2, 12489 Berlin, Germany; lia.bernabo@dlr.de, liamarta.bernabo@gmail.com
[2] McDonald Observatory and Department of Astronomy, The University of Texas at Austin, USA
[3] Earth and Planets Laboratory, Carnegie Science, 5241 Broad Branch Road, NW, Washington, DC 20015, USA
[4] NASA Goddard Space Flight Center, 8800 Greenbelt Road, Greenbelt, MD 20771, USA
[5] Center for Planetary Systems Habitability, The University of Texas at Austin, USA
[6] HUN-REN-SZTE Stellar Astrophysics Research Group, H-6500 Baja, Szegedi út Kt. 766, Hungary
[7] Department of Astronomy & Astrophysics, 525 Davey Laboratory, The Pennsylvania State University, University Park, PA 16802, USA
[8] Center for Exoplanets and Habitable Worlds, 525 Davey Laboratory, The Pennsylvania State University, University Park, PA 16802, USA
[9] ETH Zürich, Institute for Particle Physics & Astrophysics, Switzerland
[10] Anton Pannekoek Institute for Astronomy, University of Amsterdam, Science Park 904, 1098 XH Amsterdam, The Netherlands
[11] U.S. National Science Foundation National Optical-Infrared Astronomy Research Laboratory, 950 N. Cherry Avenue, Tucson, AZ 85719, USA
[12] Steward Observatory, The University of Arizona, 933 N. Cherry Avenue, Tucson, AZ 85721, USA
[13] Department of Physics & Astronomy, University of Wyoming, Laramie, WY 82070, USA
[14] Hobby Eberly Telescope, University of Texas at Austin, TX 78712, USA
[15] Electrical, Computer & Energy Engineering, University of Colorado, 425 UCB, Boulder, CO 80309, USA
[16] Department of Physics, University of Colorado, 2000 Colorado Avenue, Boulder, CO 80309, USA
[17] Department of Astronomy and Astrophysics, Tata Institute of Fundamental Research, Homi Bhabha Road, Colaba, Mumbai 400005, India
[18] Institut für Geologische Wissenschaften, Freie Universität Berlin, 12249 Berlin, Germany
[19] Department of Physics & Astronomy, University of California Irvine, Irvine, CA 92697, USA
[20] Astrophysics & Space Institute, Schmidt Sciences, New York, NY 10011, USA
[21] School of Mathematical and Physical Sciences, Macquarie University, Balaclava Road, North Ryde, NSW 2109, Australia
Received 2024 June 4; revised 2024 August 27; accepted 2024 September 21; published 2024 November 18

Abstract

We report on the discovery of a transiting giant planet around the 3500 K M3-dwarf star TOI-6383A located 172 pc from Earth. It was detected by the Transiting Exoplanet Survey Satellite and confirmed by a combination of ground-based follow-up photometry and precise radial velocity measurements. This planet has an orbital period of ∼1.791 days, a mass of $1.040 \pm 0.094\,M_J$, and a radius of $1.008^{+0.036}_{-0.033}\,R_J$, resulting in a mean bulk density of $1.26^{+0.18}_{-0.17}$ g cm^{-3}. TOI-6383A has an M dwarf companion star, TOI-6383B, which has a stellar effective temperature of $T_{\rm eff} \sim 3100$ K and a projected orbital separation of 3126 au. TOI-6383A is a low-mass dwarf star hosting a giant planet and is an intriguing object for planetary evolution studies due to its high planet-to-star mass ratio. This discovery is part of the Searching for Giant Exoplanets around M-dwarf Stars (GEMS) Survey, intending to provide robust and accurate estimates of the occurrence of GEMS and the statistics on their physical and orbital parameters. This paper presents an interesting addition to the small number of confirmed GEMS, particularly notable since its formation necessitates massive, dust-rich protoplanetary discs and high accretion efficiency (>10%).

Unified Astronomy Thesaurus concepts: Exoplanet astronomy (486); Exoplanet detection methods (489); Exoplanet formation (492); Exoplanets (498); Planet hosting stars (1242); Multiple stars (1081); Detection (1911); Radial velocity (1332)

1. Introduction

The formation of giant planets is expected to follow one of two main pathways: core accretion (CA) or gravitational instability (GI). The CA scenario (H. Mizuno 1980; J. B. Pollack et al. 1996) is a bottom-up process. Small solid particles coagulate in the protoplanetary disk, followed by the gradual growth of the planetary embryo. A phase of rapid gas accretion follows, allowing the core to acquire a massive gaseous envelope. The runaway gas accretion phase can only be triggered with a massive core ($\gtrsim 10\,M_\oplus$). This is hypothesized to take place in the Class II stage of planet formation, though simulations (G. Laughlin et al. 2004; R. Burn et al. 2021)

* Based on observations obtained with the Hobby–Eberly Telescope (HET), which is a joint project of the University of Texas at Austin, the Pennsylvania State University, Ludwig-Maximillians-Universitaet Muenchen, and Georg-August Universitaet Goettingen. The HET is named in honor of its principal benefactors, William P. Hobby and Robert E. Eberly.

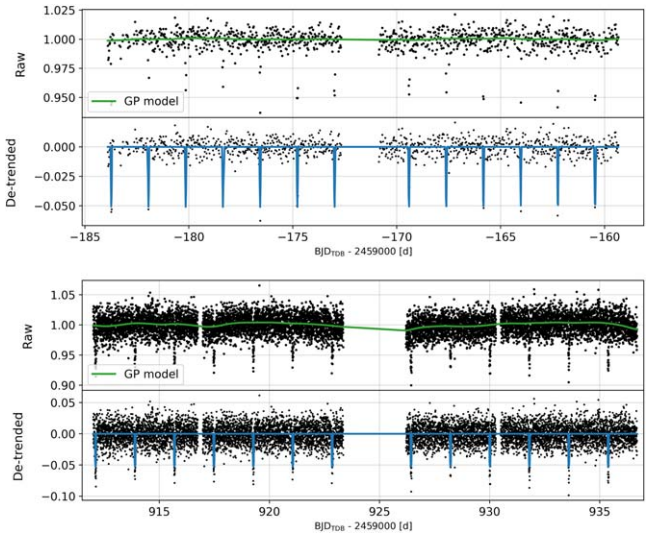

Figure 1. TESS transits observed in Sectors 19 and 59 excluding masked data points, modeled with GP. The exposure times are 1800 s and 200 s, respectively.

suggested that this mechanism for forming giant planets might suffer from a problem of mass-budget and formation timescales around M dwarfs. Theoretical models predict that the timescale for the formation of Jupiter-like gas giants could exceed the lifespan of the gas disk (see G. Laughlin et al. 2004 and references therein), hinting at the possibility of alternative processes in the formation of massive gas giant planets around M dwarf stars.

On the other hand, the GI theory of planet formation (A. P. Boss 1997) consists of a rapid formation mechanism that involves the breakup of a massive protostellar disk into clumps under self-gravity. These clumps subsequently undergo contraction and collapse to give rise to giant planets or substellar objects. In the outer regions of the disk, far beyond the ice line, GI has been hypothesized to be able to form giant planets around M dwarfs (A. P. Boss 2006, 2011; A. Mercer & D. Stamatellos 2020; A. P. Boss & S. Kanodia 2023). The formation is then supposed to be followed by migration because of the interaction with the disk. This scenario takes place during the Class 0 or I disk phase, quite early in the life of the disk when it is much more massive (Ł. Tychoniec et al. 2020).

Characterizing and cataloging the growing sample of Giant Exoplanets around M dwarf Stars (GEMS; transiting with planetary radius $\gtrsim 8\ R_{\oplus}$, orbiting M dwarf stars with $T_{\rm eff} \leqslant 4000$ K) may reconcile the existence of this sample with the two contemporary theories of giant planet formation. This is the goal of the Searching for GEMS survey (S. Kanodia et al. 2024a) aiming to explore recent discoveries of GEMS and assess them in light of existing theories of planet formation. S. Kanodia et al. (2024a) carried out an exhaustive discussion on the occurrence and formation of GEMS and showed that approximately 40 GEMS with 5σ mass measurements are required to better quantify the significance of potential trends between stellar mass and bulk density for giant planets. The required sample size is almost double the current ∼25 planet sample. Identified candidates are undergoing concurrent validation and follow-up observations by ground-based telescopes (photometric and spectroscopic surveys) to confirm their planetary status and determine their stellar and planetary characteristics.

In this manuscript, we present the detection of a giant planet around the M3 spectral type dwarf star TOI-6383A. The discovery was made using the Transiting Exoplanet Survey Satellite (TESS), and a ground-based program of observations followed to characterize the system. In particular, we obtained six ground-based transits with Red Buttes Observatory (RBO; D. H. Kasper et al. 2016), in Wyoming, USA, along with precise Radial Velocities (RVs) from the Habitable-zone Planet Finder (HPF; S. Mahadevan et al. 2012, 2014). TOI-6383A has a companion M dwarf at a projected distance of ∼18″ (31026 au) away. TOI-6383B has a M5 spectral type and an effective temperature of 3121±81 K.

The paper is structured as follows: in Section 2, we describe the photometric and spectroscopic observations of TOI-6383A; in Section 3, we report our investigations on the characteristics of the host star and its companion star TOI-6383B; in Section 4, we describe the joint transit and RV fitting procedure and the results on the planetary and orbital parameters, and in Section 5, we put the planet in context and discuss its interior and formation.

2. Observations

2.1. Transit Light Curves

2.1.1. TESS

TOI-6383A (TIC-328513434, Gaia Data Release 3 4739340117330498 56, R.A. $\alpha_{J2016} = 04{:}01{:}41.93$, decl. $\delta_{J2016} = 60{:}53{:}28.89$) was observed by TESS (G. R. Ricker et al. 2015) in Sector 19 in Camera 2 starting in the night of 2019 December 28 and observing the target for 27 days, as part of the broader efforts in the TESS Faint-star Search, which identified 1617 new transiting-planet candidates around fainter stars, to improve our understanding of giant, close-in exoplanets, with the usage of the Quick- Look Pipeline (M. Kunimoto et al. 2022). The images were acquired with an 1800 s exposure time. Starting on 2022 November 26 TOI-6383A was re-observed in Sector 59 in Camera 2 with a 200 s exposure time. We generate the light curve (LC) from the TESS full-frame images (FFIs) by employing the open-source tool `eleanor` (A. D. Feinstein et al. 2019). This software utilizes the `TESScut` service to capture a 31 × 31 pixel excerpt from the calibrated FFIs, centered on TOI-6383A. The LC is computed from the `CORR_FLUX` values, employing linear regression with factors such as the pixel position, background measurement, and time to eliminate correlated signals. We use the default `eleanor` aperture, resulting in a differential photometric precision of 4332 ppm and 10014 ppm for Sectors 19 and 59, respectively.

The `eleanor` aperture includes numerous field stars, contributing to the photometric dilution observed in the TESS light curve. This necessitates subsequent ground-based follow-up to resolve these background stars.

Figure 1 shows the raw and detrended TESS photometry of both sectors, modeled with Gaussian process (GP) regression, which is described more in Section 4.

We perform ground-based photometric and spectroscopic follow-ups to confirm the presence of the planet and characterize its properties.

2.1.2. Ground-based Photometric Observations

Between 2023 August and November, we observed six transits of TOI-6383Ab with the 0.6 m telescope located at

Table 1
Summary of the Main Properties of the Ground-based Follow-up Program at RBO

Obs. date UT (DD-MM-YY)	PSF FWHM min–max (″)	Air mass start–mid–end
21-08-2023	1.84–2.54	2.02–1.34–1.10
30-08-2023	1.88–2.75	2.15–1.41–1.16
08-09-2023	2.08–3.20	2.30–1.33–1.08
26-09-2023	1.79–2.87	2.66–1.59–1.17
30-10-2023	1.80–2.96	1.55–1.09–1.16
15-11-2023	1.83–2.32	1.13–1.07–1.23

Note. In the second column, we report the minimum and maximum values of the FWHM during the night. In the last column, we report the air mass at the beginning, in the middle of the observations, and at the end of the night.

Table 2
Binned RV Data Points of TOI-6383A Acquired by HPF: Time in BJD_{TDB}, RV, and Error Bar on RV

Time BJD_{TDB} - 2 460 000 [d]	RV ($m\,s^{-1}$)	σ_{RV} ($m\,s^{-1}$)
182.954575	−352	32
187.938320	−38	43
190.910754	165	45
192.921425	180	31
194.900860	52	53
196.893194	−157	60
197.894106	58	47
215.868385	112	46
215.995449	167	40
225.986554	−408	41

RBO (D. H. Kasper et al. 2016), Wyoming, USA. The telescope is an $f/8.43$ Ritchey–Chrétien Cassegrain, currently equipped with an Apogee Alta F16 camera, and constructed by DFM Engineering, Inc. The transits were observed with the Bessell I filter (M. S. Bessell 1990) and 240 s exposure times and a field of view of $8.94 \times 8.'94$. Table 1 shows a summary of the main properties of the data acquisition of the photometric follow-up program. The FWHM of the source in RBO photometry ranges from approximately 1.8 to 3.2 pixels, while the scale is $0.''72\,pixel^{-1}$. Therefore, the aperture sizes of RBO photometry are enough to estimate and correct for dilution in the TESS photometry after careful aperture selection and avoid contamination of the 18″ away companion star TOI-6383B in the RBO photometry.

The RBO data are processed using the `Python` package `astropy` (Astropy Collaboration et al. 2013) to perform bias, dark, and flat-field processing. Astrometry information is verified (or added if missing) using the `astrometry.net` package (D. W. Hogg et al. 2008). Aperture photometry is performed using `Python photutils` (L. Bradley et al. 2023) at the locations (corrected for proper motions) of all Gaia sources (brighter than $G = 17$ mag using `astroquery`) with multiple apertures at once. Using the Gaia coordinates allows for easy and consistent identification and cross-matching. The midpoints of the exposures are converted to BJD_{TDB} using `barycorrpy` (S. Kanodia & J. Wright 2018), a `Python` implementation of algorithms by J. Eastman (2012). To perform relative photometry, the flux from the target star is compared to the sum of the fluxes of the selected comparison stars that are chosen to: be present on all frames, have no nearby companions, and not be known variables. The final choice of aperture was made by minimizing the scatter in the data. Further refinement of comparison stars is done by manually (de)selecting stars to yield consistent light curves across all defined apertures. These light curves are shown after modeling in Figure 4 along with the two TESS transits.

2.2. RV Follow-up with HPF

We also acquired 10 radial velocity visits of TOI-6383A with HPF (S. Mahadevan et al. 2012, 2014, 2018), a near-infrared, stabilized (G. Stefansson et al. 2016), fiber-fed (S. Kanodia et al. 2018), high-resolution ($R \sim 50\,000$) radial velocity spectrograph (A. J. Metcalf et al. 2019) located at the 10 m Hobby–Eberly Telescope (HET; L. W. Ramsey et al. 1998; G. J. Hill et al. 2021) at McDonald Observatory in Texas, USA. The instrument bandpass covers the range from 8080 to 12780 Å.

The high-resolution spectra were acquired between 2023 August and October. Ten visits were made to the target to obtain a full-phase RV curve. Each visit consists of two exposures of 969 s each, where the signal-to-noise (S/N) per pixel per unbinned exposure ranges between a minimum of ∼21 and a maximum of ∼32 at 1070 nm. The two RV data points acquired each night are binned by weighted averaging to improve the S/N. The error bar is then calculated as the harmonic mean of the squared error bars on the single measurements. The binned RVs are reported in Table 2 and shown phase-folded in Figure 5.

We use the algorithms described in the tool `HxRGproc` (J. P. Ninan et al. 2018) for bias removal, nonlinearity correction, cosmic-ray correction, slope/flux, and variance image calculation of the raw HPF data.

We utilize the template-matching method (e.g., G. Anglada-Escudé & R. P. Butler 2012) to derive radial velocities from the collected spectra. This method is incorporated within the `SpEctrum Radial Velocity AnaLyser` pipeline (M. Zechmeister et al. 2018), customized for HPF (A. J. Metcalf et al. 2019). Initially, a master template is constructed based on all HPF observations of TOI-6383A. Subsequently, for each individual observation, we ascertain the Doppler shift by adjusting its velocity to minimize the χ^2 when compared against the template. The telluric regions are identified using a synthetic telluric-line mask generated by `telfit` (K. Gullikson et al. 2014), a Python interface for the line-by-line radiative transfer model package (S. A. Clough et al. 2005). After excluding the telluric and sky-emission lines, the master template is formed using HPF observations of the target star. To compensate for the barycentric motion in the individual spectra, we use the barycentric correction algorithms of J. T. Wright & J. D. Eastman (2014), implemented in the `Python` package `barycorrpy` (S. Kanodia & J. Wright 2018).

2.3. High-contrast Imaging: NN-Explore Exoplanet Stellar Speckle Imager

TOI-6383A was observed with the NN-Explore Exoplanet Stellar Speckle Imager (NESSI; N. J. Scott et al. 2018) on the WIYN Observatory[22] on 2023 September 9. Sequences of diffraction-limited frames were taken in the Sloan Digital Sky

[22] The WIYN Observatory is a joint facility of the NSF's National Optical–Infrared Astronomy Research Laboratory, Indiana University, the University of Wisconsin–Madison, Pennsylvania State University, Purdue University, and Princeton University.

Survey (SDSS) r' and z' filters and processed following the methods described in S. B. Howell et al. (2011) to create high-resolution, reconstructed speckle images. We show the reconstructed images along with the achieved contrast limits as a function of the angular separation in Figure 2. The NESSI results exclude the presence of nearby sources at 5σ confidence down to relative magnitude limits of $\Delta r' = 3.96$ mag and $\Delta z' = 3.66$ mag at a separation of $0\farcs2$ and limits of $\Delta r' = 4.55$ mag and $\Delta z' = 4.38$ mag at a separation of $1\farcs2$.

2.4. LRS-2

To verify the spectral type and stellar characteristics of TOI-6383A, we conducted observations of the target using the second-generation low-resolution spectrograph (LRS-2; H. Lee et al. 2010; T. S. Chonis et al. 2016) at HET located at McDonald Observatory in Texas, USA. LRS-2 is an optical integral field unit spectrograph with low resolution ($R \sim 1900$), comprising two arms that simultaneously capture two fields of view measuring $6'' \times 12''$ each, with a separation of $100''$. The red arm (LRS-2-R) comprises two channels covering ~6430–8450 Å and ~8230–10560 Å, while the blue arm (LRS-2-B) is equipped with a pair of channels covering spectral ranges of ~3640–4670 Å and ~4640–7000 Å. We collected spectra with LRS-2-B on 2024 February 17, with a seeing of $1\farcs4$ and exposure times of 1800 s.

The raw LRS-2 data are initially processed with `Panacea`,[23] which carries out bias subtraction, dark subtraction, fiber tracing, fiber wavelength evaluation, fiber extraction, fiber-to-fiber normalization, source detection, source extraction, and flux calibration for each channel. The absolute flux calibration comes from default response curves and measures of the mirror illumination as well as the exposure throughput from guide images.

Following the initial reduction process, we employed `LRS2Multi`[24] for advanced reduction steps and calibration of `Panacea` products. We pinpointed the target star, defined a $3\farcs5$ aperture, and utilized fibers beyond this aperture to construct our sky model for each exposure. Subsequently, we subtracted the initial sky and generated a principal component basis consisting of 25 components from the residuals to eliminate further sky residuals caused by variable spectral point spread functions (PSFs) for each fiber. The target spectrum was then extracted from the sky-subtracted frames and the resulting LRS-2 spectra of TOI-6383A were utilized to estimate the star's spectral type, as described in Section 3.3.

3. Stellar Parameters

3.1. A Companion Star: TOI-6383B

We searched the catalog of the second and third Gaia data releases (DR2, DR3; Gaia Collaboration 2016, 2018, 2023) for possible comoving companions to TOI-6383A. We searched all objects within $60''$ of the target, which corresponds to a physical separation of around 10^4 au at the distance of TOI-6383A. We selected the only object with comparable proper motions (PM), Gaia DR2 ID 473934007432818688. The star is ~3 mag fainter in the G band, has parallax and coordinates PM_α and PM_δ, which only slightly differ from that of TOI-6383A. They are listed in Table 3. This putative M dwarf companion is found at a separation of $\sim 18''$ from TOI-6383A, which corresponds to a spatial projected separation of ~3100 au.

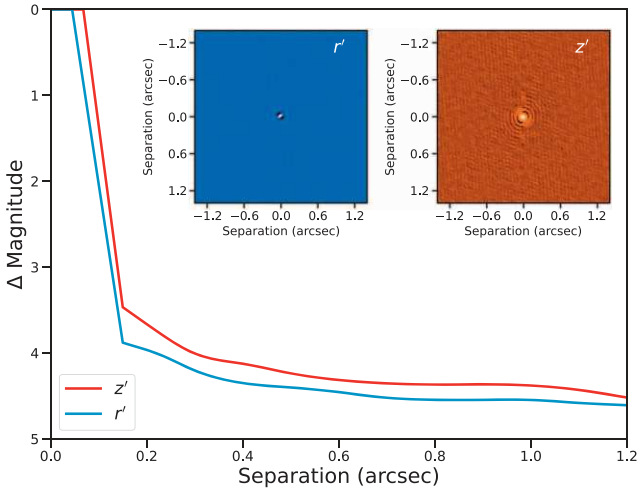

Figure 2. Reconstructed NESSI speckle images and 5σ contrast curves for TOI-6383A. Observations were taken simultaneously in the r' filter with the blue camera (upper left inset image) and the z' filter with the red camera (upper right inset image). The contrast curves indicate the limiting magnitude difference at which bound or background sources could be detected for separations between $0\farcs2$ and $1\farcs2$. Note that the stellar companion falls outside the field of view.

TOI-6383A and TOI-6383B are present also in the catalog of K. El-Badry & H.-W. Rix (2018) for Gaia Data Release 2, implying that the line-of-sight difference between the two objects in distance is less than twice their projected separation (within 3σ limit). Moreover, they have proper motion differences within 3σ of the maximum velocity difference expected for a system of total mass 5 $M_\odot$ with circular orbits, meaning that the proper motion of the two stars is consistent with a bound Keplerian orbit.

Based on the parallax and absolute K_s magnitude, TOI-6383B is lower in mass than our planet host TOI-6383A and hence referred to as TOI-6383B from now on.

3.2. TOI-6383A and B Stellar Parameters

The stellar parameters are derived using a combination of Gaia astrometry, LRS-2 spectra, and photometric relations, and are summarized in Table 3.

The separation of the two stars in the binary system is far enough that TOI-6383A is clearly resolved in the Two Micron All Sky Survey (2MASS; M. F. Skrutskie et al. 2006) images, hence we could use the photometric relations to derive the mass and radius of both TOI-6383A and TOI-6383B. In more detail, we use the absolute K_s magnitude to derive the radii (A. W. Mann et al. 2015), and from them, the stellar masses using the empirically calibrated sample from A. Schweitzer et al. (2019). As indicated in A. W. Mann et al. (2015), the error bars on the radii are incremented by 2.89% to account for the systematic scatter. These parameters are reported in Table 3.

We use the `HPF-SpecMatch`[25] routine (G. Stefansson et al. 2020) to calculate the stellar parameters from HPF spectra. The template-matching method is based on `Spec-Match-Emp` from S. W. Yee et al. (2017) and compares the target spectrum with the HPF spectral library, containing 166

[23] https://github.com/grzeimann/Panacea
[24] https://github.com/grzeimann/LRS2Multi
[25] https://gummiks.github.io/hpfspecmatch/

Table 3
Stellar Parameters for Both TOI-6383A and TOI-6383B

Parameter	Symbol [units]	TOI-6383A	TOI-6383B	Reference
Identifiers				
TESS Input Catalog	TIC	328513434	328513444	...
TESS Object of Interest	TOI	6383.01	...	...
2MASS	...	J04014183 + 6053297	J04014299 + 6053457	...
Gaia identifier	DR2	473934011733049856	473934007432818688	GAIA DR2
WISE	...	J040141.89 + 605329.2	J040143.05 + 605345.3	WISE[a]
Coordinates				
R.A.	R.A. (α_{J2016}) [h:m:s]	04:01:41.9293	04:01:43.0906	GAIA DR3
decl.	decl. (δ_{J2016}) [deg]	60:53:28.89	60:53:44.97	GAIA DR3
Apparent separation (of B from A)	[″]	...	18.16552 ± 0.00023	GAIA DR3
Parallax	ϖ [mas]	5.847 ± 0.031	6.10 ± 0.16	GAIA DR3
Distance from Earth	d [pc]	$172.08^{+0.91}_{-0.82}$	$182.09^{+5.5}_{-6.2}$	GAIA DR3
Projected physical separation (of B from A)	[au]	...	3126 ± 17	GAIA DR3
Proper motion	pmRA [mas yr^{-1}]	41.023 ± 0.035	41.02 ± 0.17	GAIA DR3
Proper motion	pmDec [mas yr^{-1}]	-51.30 ± 0.032	-51.28 ± 0.16	GAIA DR3
Magnitudes				
Johnson B	B [mag]	18.52 ± 0.16	...	APASS[b]
Johnson V	V [mag]	16.63 ± 0.20	...	APASS
J	J [mag]	12.985 ± 0.026	15.174 ± 0.053	2MASS
H	[mag]	12.318 ± 0.017	14.775 ± 0.069	2MASS
K_s	[mag]	12.087 ± 0.021	14.222 ± 0.071	2MASS
Gaia	G [mag]	15.66280 ± 0.00067	18.5239 ± 0.0018	GAIA DR3
TESS	T [mag]	14.4506 ± 0.0073	17.064 ± 0.010	TESS
WISE 3.4 μm	W1 [mag]	11.967 ± 0.024	14.134 ± 0.029	WISE
WISE 4.6 μm	W2 [mag]	11.860 ± 0.022	13.945 ± 0.038	WISE
WISE 12 μm	W3 [mag]	11.61 ± 0.20	12.715	WISE
WISE 22 μm	W4 [mag]	9.184	8.678	WISE
Gaia $B_P - R_P$ color	G_{BP}-G_{RP}	2.5110 ± 0.0089	3.310 ± 0.076	GAIA DR3
Stellar parameters				
Radius[c]	$R_\star$ [$R_\odot$]	0.457 ± 0.019	$0.217^{+0.017}_{-0.019}$	This work
Mass[d]	$M_\star$ [$M_\odot$]	0.458 ± 0.011	0.205 ± 0.008	This work
Mean density	$\rho_\star$ [g cm^{-3}]	6.74 ± 0.35	25.62 ± 5.59	This work
Effective temperature	$T_{\rm eff}$ [K]	3444 ± 88[e]	3121 ± 81[f]	This work
Surface gravity[e]	$\log_{10}(g)$ [cgs]	4.81 ± 0.05	...	This work
Luminosity	$L_\star$ [$L_\odot$]	0.0326 ± 0.0009	0.0042 ± 0.0005	This work
Stellar type		M3[g h]	M5[g]	This work
Other stellar parameters				
V sin (i)[e]	[km s^{-1}]	<2.0	...	This work
Absolute radial velocity	[km s^{-1}]	11.9 ± 0.3	...	GAIA DR3
Galactic velocities (barycentric r. s.)	U, V, W [km s^{-1}]	-40.07 ± 1.11, -35.57 ± 1.44, -7.53 ± 0.31	...	This work
" " (LSR)	U, V, W [km s^{-1}]	-28.97 ± 1.39 , -21.33 ± 1.59, -0.28 ± 0.68	...	This work

Notes. All reported magnitudes are apparent. Three dots "..." indicate that the parameter is not calculated or not available.
[a] Wide-field Infrared Survey Explorer (E. L. Wright et al. 2010).
[b] AAVSO Photometric All-Sky Survey (A. A. Henden et al. 2018).
[c] From its relation with the absolute K_s magnitude (A. W. Mann et al. 2015; see Section 3.2)
[d] Equation (6) from A. Schweitzer et al. (2019), based on the empirically calibrated sample; see Section 3.2.
[e] Calculated with the `HPF-SpecMatch` algorithm (G. Stefansson et al. 2020; see Section 3.2).
[f] Equation (11) from M. Rabus et al. (2019);
[g] From Gaia colors relations from R. Kiman et al. (2019), as described in Section 3.3.
[h] Estimated with LRS-2 spectra; see Section 3.3.

stars in the following parameter ranges for the effective temperature $T_{\rm eff} = [2700\,{\rm K},\ 6000\,{\rm K}]$, surface gravity $\log(g) = [4.3,\ 5.3]$, and metallicity $[{\rm Fe/H}] = [-0.5,\ +0.5]$ dex. The spectrum of the target is compared with each spectrum from the library, returning its χ^2. This determines the library stars ranking, as a first comparison method. Afterward, only the top five library stars with the best χ^2 values are taken into consideration. The χ^2 metric is then employed to allocate scaling constants to each of these five best-fit library stars. This process results in the creation of a composite spectrum that closely aligns with the target spectrum. The scaling constants are instrumental in determining a weighted average, which facilitates precise parameter estimations for the target star's spectroscopic parameters. Following G. Stefansson et al. (2020), we use a leave-one-out cross-validation approach to determine the error bars on these parameters. In this process, a library star of interest is removed from the rest of the stellar library pool. Then, the algorithm is executed again to infer its stellar parameters independently of its true parameters. The differences between these calculated parameters and the true parameter values are used to estimate the uncertainty of inferred parameters.

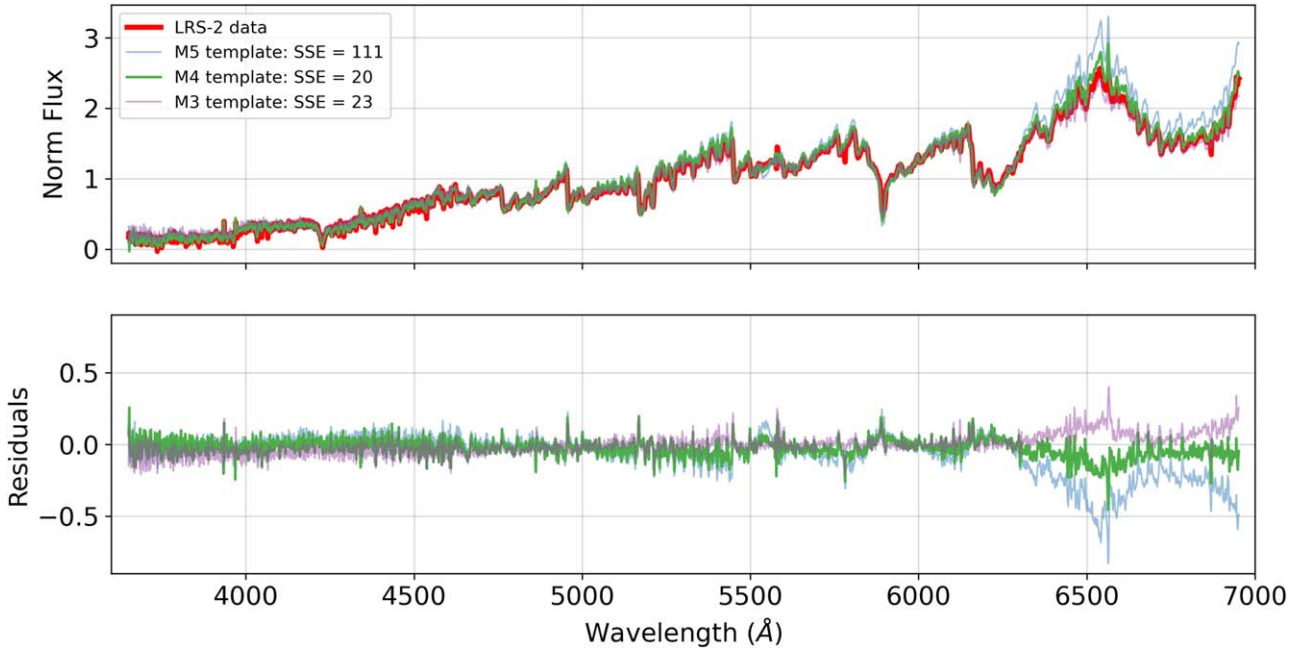

Figure 3. Comparison of the LRS-2 spectra with the empirical templates from `pyHammer`. The observed LRS-2-B spectra after response and telluric correction are plotted in red. Empirical templates of M3, M4, and M5 stars are also shown. The summed square errors (SSE) are reported in the legend. Along with the residuals (bottom part of the Figure), they show that the M3-4 stellar spectra are the best-matching ones.

The calculated stellar parameters for TOI-6383A from HPF spectra are reported in Table 3. Since we obtained no separate HPF observation of TOI-6383B, its effective temperature is calculated from its relation with the Gaia G magnitude (Equation (11) from M. Rabus et al. 2019).

Due to the HPF spectral resolution limit, we can only determine an upper limit on v sin i for TOI-6383A. We also determine metallicity using two methodologies but note that the determination of the metallicity of M dwarfs is challenging and has many caveats. Due to the lower temperature of the atmospheres of M dwarf stars, they are characterized by molecular features. Unfortunately, this introduces complexities in determining their line profiles and metallicity.

The first method makes use of with `HPF-SpecMatch`, which resulted in $[\mathrm{Fe/H}] = 0.15 \pm 0.12$ dex. However, the estimate is not reliable because of the multiplicity of the minima in the χ^2 minimization, making the parameter space "flat" with the stellar metallicity.

We also estimated the metallicity of TOI-6383A using Gaia colors and the online tool `METaMorPHosis`[26]—provided by C. Duque-Arribas et al. (2023)—which derives several photometric calibrations of metallicity. We used G absolute Gaia magnitude, $B_P - R_P$ Gaia color, and J, H, and K 2MASS absolute magnitudes, as reported in Table 3. The weighted mean among three estimates made with $B_P - R_P - G$, $B_P - R_P - J$, and $B_P - R_P - H$ planes is $[\mathrm{Fe/H}] = 0.20 \pm 0.08$ dex, which is consistent with the `HPF-SpecMatch` estimate within the error bars.

We computed the Lomb–Scargle periodogram on the stellar photometry to check the presence of stellar rotation. We applied it on the Zwicky Transient Facility (E. C. Bellm et al. 2019; M. J. Graham et al. 2019), with 521 photometric measurements with the r filter spanning ∼2000 days and on the All-Sky Automated Survey for Supernovae (B. Shappee et al. 2014; T. Jayasinghe et al. 2019) survey 164 available V-magnitude measurements spanning ∼1400 days. We could not find any periodicity above the 10% false-alarm probability limit.

In the context of galactic kinematics, we calculated the U, V, and W velocities of TOI-6383A in the barycentric and local standard of rest frames using the `Python` package `galpy` (J. Bovy 2015) and the relations from R. Schönrich et al. (2010). They are reported in Table 3. Using the criterion from T. Bensby et al. (2014), we can classify TOI-6383A as a thin disk star.

3.3. Spectral Classification

To compute the spectral classification of TOI-6383A with the LRS-2 spectra, we used the `Python` package `pyHammer` (A. Kesseli et al. 2017; B. R. Roulston et al. 2020), which is based on `The Hammer` (K. R. Covey et al. 2007) and estimates of the spectral type, metallicity, and RV, and is also to visually classify stellar spectra. We compare the observed spectrum with spectral line index measurements and template optical spectral templates. These are derived from the MaNGA Stellar Library, consisting of calibrated optical spectra from SDSS IV (R. Yan et al. 2019). From this comparison, we obtained a spectral type M3-4 (see Figure 3, and, in particular, the comparison between the residuals in the ∼6200–7000 Å range in the bottom plot).

We also compare Gaia colors $B_P - R_P$, $B_P - G$, and $G - R_P$ with Table 4 of R. Kiman et al. (2019) to obtain the spectral type of both stars, obtaining M3 spectral type for TOI-6383A and M5-6 for TOI-6383B.

We therefore adopt M3 as the spectral type of TOI-6383A, given that it matches the results from R. Kiman et al. (2019) and that the summed square errors of M3 and M4 templates are similar.

4. Data Analysis: Joint Fit of LCs and RVs

We perform a joint fitting of the reduced two TESS and six ground-based transit LCs and RV data using the `Python`

[26] https://chrduque.shinyapps.io/metamorphosis/

Table 4
Orbital, Transit, and Planetary Parameters Based on the `exoplanet` Package Solution

Parameter	Symbol,	units	Value
Orbital Parameters			
Orbital period	P	[d]	$1.79058695^{+8.7e-7}_{-8.6e-7}$
Eccentricity†	e	...	$0.050^{+0.042}_{-0.033}$, $^{+0.086}_{-0.047}$
Periastron angle	ω	...	$0.42^{+1.26}_{-1.08}$ rad $= 23.8^{+72}_{-62}$°
Semimajor axis	a	[au]	0.02292 ± 0.00037
RV Semi-amplitude	K	[m s^{-1}]	277 ± 23
RV offset velocity[a]	γ	[m s^{-1}]	-81 ± 19
RV trend	$\dot{\gamma}$	[m s^{-1} yr^{-1}]	-30 ± 97
RV jitter	$\sigma_{\rm RV}$	[m s^{-1}]	31^{+26}_{-21}
Orbital inclination	i	[°]	$88.80^{+0.78}_{-0.68}$
Transit Parameters			
Transit mid-time	T_c	[BJD$_{\rm TDB}$]	$2459933.59545^{+2.0e-4}_{-2.1e-4}$
Transit duration	T_{14}	[d]	$0.0641^{+0.0020}_{-0.0017}$
Scaled radius	R_p / $R_\star$	...	$0.2245^{+0.0042}_{-0.0041}$
Scaled semi-major axis	a / $R_\star$	...	10.68 ± 0.32
Photometric jitter[b]	$\sigma_{\rm TESS\ 19}$	[ppm]	6524^{+160}_{-150}
	$\sigma_{\rm TESS59}$	[ppm]	14901^{+109}_{-107}
	$\sigma_{\rm RBO2108}$	[ppm]	8432^{+1505}_{-1420}
	$\sigma_{\rm RBO3008}$	[ppm]	47^{+650}_{-44}
	$\sigma_{\rm RBO0809}$	[ppm]	72^{+1047}_{-68}
	$\sigma_{\rm RBO2609}$	[ppm]	52^{+723}_{-48}
	$\sigma_{\rm RBO3010}$	[ppm]	46^{+574}_{-43}
	$\sigma_{\rm RBO1511}$	[ppm]	91^{+1762}_{-87}
Dilution[c] [d]	$D_{\rm TESS\ 19}$	...	$0.882^{+0.042}_{-0.040}$
	$D_{\rm TESS59}$	...	0.894 ± 0.032
Planetary Parameters			
Mass	M_p	[M_J]	1.040 ± 0.094
	M_p	[$M_\oplus$]	331 ± 30
Radius	R_p	[R_J]	$1.008^{+0.036}_{-0.033}$
	R_p	[$R_\oplus$]	$11.29^{+0.41}_{-0.37}$
Density	ρ_p	[g cm^{-3}]	$1.26^{+0.18}_{-0.17}$
Planetary insolation	S	[$S_\oplus$]	51.3 ± 6.3
Equilibrium temperature[e]	$T_{\rm eq}$	[K]	745 ± 23

Notes. The reported error bars in the third and fourth columns correspond to 1σ uncertainty, while † both 1σ and 2σ confidence levels are reported for the eccentricity.
[a] In addition to the absolute RV in Table 3.
[b] Jitter added in quadrature to photometric instrument error separately for each transit.
[c] Dilution due to the presence of background stars in the TESS aperture is not accounted for in the `eleanor` incident flux.
[d] We assume the planet to be a blackbody with zero albedo and perfect energy redistribution to estimate the equilibrium temperature.

package `exoplanet` (D. Foreman-Mackey et al. 2021). It utilizes `PyMC3`, a Hamiltonian Monte Carlo posterior sampling algorithm (J. Salvatier et al. 2016).

Each photometry data set is fitted with separate quadratic analytic limb darkening coefficients, using the parameterization of D. M. Kipping (2013). Additionally, we incorporate a white noise model by including a jitter term for each ground-based photometry data set. In the case of the TESS photometry, we include a dilution term to account for the presence of blended or spatially unresolved nearby background stars. The dilution term is adjusted individually for each TESS sector, as the positioning of the target and background stars on the camera pixels varies. In contrast, given the PSF and aperture size are much smaller than the separation from the companion, we assume that the ground-based photometry from the RBO transits remains uncontaminated. Moreover, the likelihood function for the TESS photometry includes a GP kernel to model the quasiperiodic signal, which is likely an artifact from the photometry reduction of the FFI (see S. Kanodia et al. 2022 for more details). The separate rotation kernels result in a recurrence timescale of $6.37^{+6.37}_{-4.49}$ days in the Sector 19 data set and $11.63^{+1.97}_{-2.33}$ days in the Sector 59 data set.

The RV curve is fitted with a Keplerian model, allowing the eccentricity to vary. Additionally, we incorporate an RV offset and jitter term specific to HPF, as well as a linear RV trend to accommodate long-term drifts, encompassing both instrumental and astrophysical factors, such as the presence of an additional planetary companion. Convergence is checked using the Gelman–Rubin statistic, satisfying $\hat{R} \leqslant 1.1$ (A. Gelman & D. B. Rubin 1992; E. B. Ford 2006). The planetary parameters derived from the joint fit are shown in Table 4. The planet is on a 1.791 day orbit around TOI-6383A, at a scaled distance of $a / R_\star = 10.86 \pm 0.32$. It has a mass of 1.040 ± 0.094 M_J and a radius of $1.008^{+0.036}_{-0.033}$ R_J. The fitted TESS and ground-based light curves are in Figure 4, while the phase-folded RV curve can be found in Figure 5, along with the residuals from the fit.

To confirm these results, we also performed a joint analysis on the RV data and the TESS and ground-based transits with the `idl` script Transit Light Curve Modeller[27] (Sz. Csizmadia 2020) to have an independent check of the results of the planet and system parameters. The photometric noise model is based on a wavelet model by J. A. Carter & J. N. Winn (2009), extended by Sz. Csizmadia et al. (2023). For this specific analysis, it has been implemented to model multiple band transit observations. All parameters fitted with the two aforementioned scripts agree within 2σ, confirming the previous results.

5. Discussion

5.1. TOI-6383Ab in Context

TOI-6383Ab joins the short but growing list of GEMS. Due to the small sample size of confirmed GEMS, it is still hard to make robust conclusions regarding trends in their planetary and orbital parameters. This planet is found as part of the Searching for GEMS survey and allows us to delve deeper into the statistics of the ∼25 transiting GEMS discovered up to this date (see the complete list in Table 1 in S. Kanodia et al. 2024a).

TOI-6383Ab is a Jupiter-like giant planet with a radius of $1.008^{+0.036}_{-0.033}$ R_J, a mass of 1.040 ± 0.094 M_J, and a mean density of $1.26^{+0.18}_{-0.17}$ g cm^{-3}. Using the NASA Exoplanet Archive (R. L. Akeson et al. 2013) database, in Figure 6 we put TOI-6383Ab in context by plotting it in parameters spaces together with all known GEMS and giant planets around F-, G-, and K-type stars. Chosen planets as GEMS are in the following range of parameters: stellar mass [0.30, 0.65] $M_\odot$, effective temperature [3000, 4000] K, planetary mass [40,900] $M_\oplus$, and radius >8 $R_\oplus$.

TOI-6383Ab is similar to TOI-5205 b (S. Kanodia et al. 2023; both highlighted in the two diagrams in 6) in terms of planetary mass (1.04 M_J and 1.08 M_J, respectively) and radii (1.01 R_J and 1.03 R_J, respectively)—and consequently mean

[27] http://www.transits.hu/

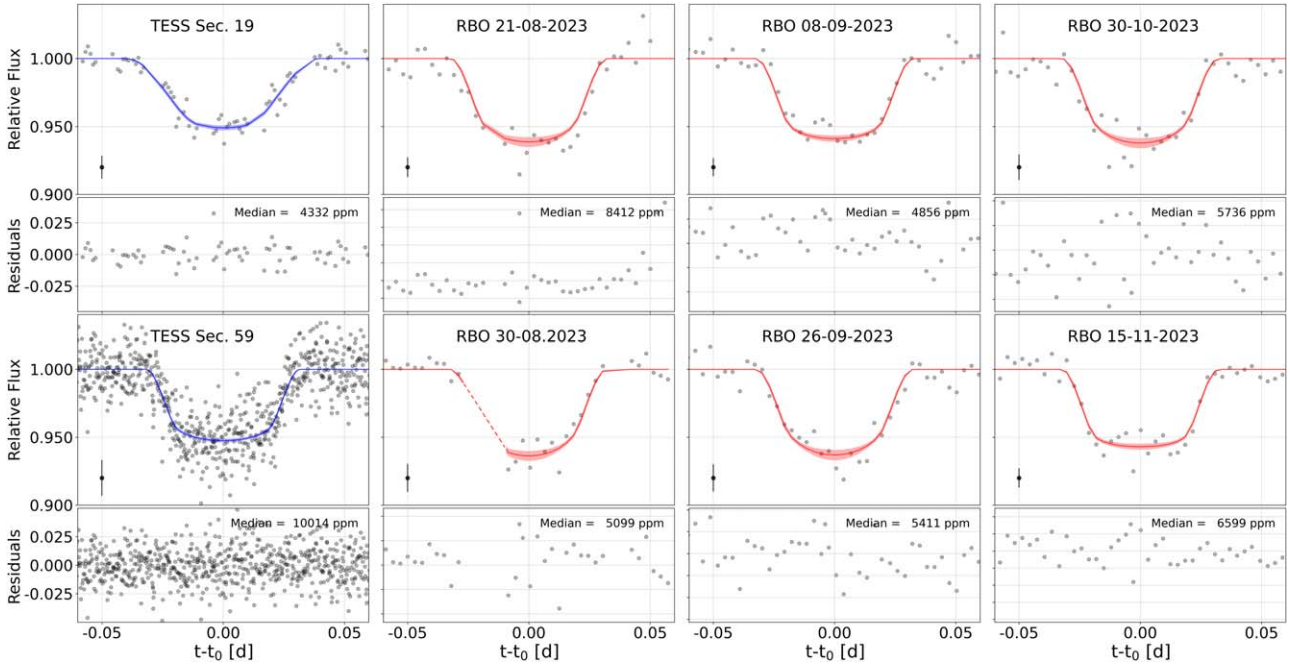

Figure 4. TESS and RBO light curves fitted by `exoplanet` jointly with RVs, with a focus on the transit region. Time is subtracted from the transit mid-time for each light curve. In all plots, the detrended data are in gray, and the model and 16%–84% confidence levels are in blue (for TESS transits) and red (for ground-based transits). In each upper plot, the point at $x = -0.05$ represents the median uncertainty in the photometric data.

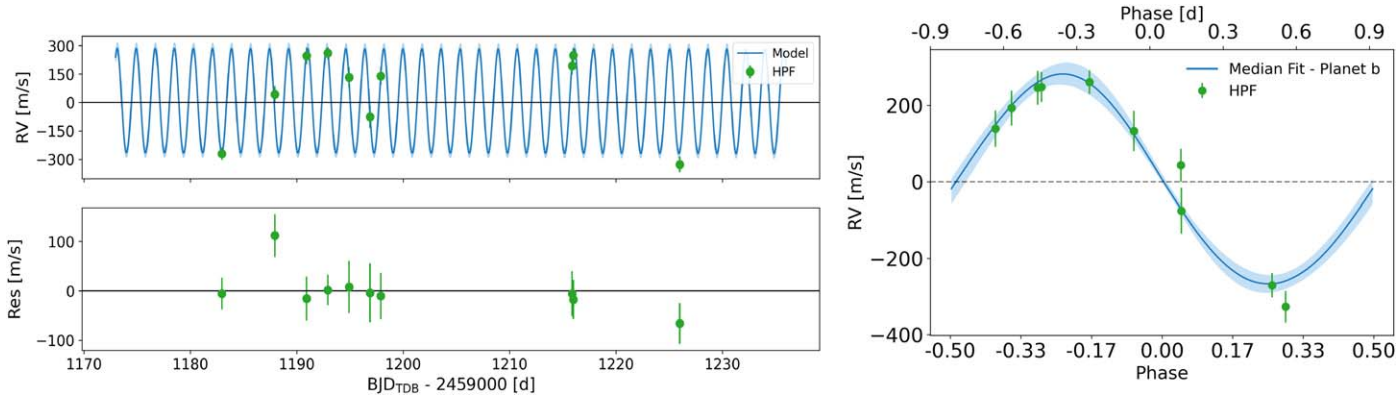

Figure 5. Left: time series of the HPF RV data and their residuals after subtracting the best-fitting model. The best-fitting model derived from the RV–photometry joint fit is plotted in blue and the 16%–84% confidence interval is in light blue. We show data binned by night in green. Residuals of the fit are plotted in the bottom plot below the time series. Right: phase-folded HPF RV curve of TOI-6383.

density—and equilibrium temperature (745 K and 737 K, respectively).

The upper panel in Figure 6 shows the relation between planetary mass and planetary radius, colored by stellar mass. The 0.3 g cm^{-3}, 1 g cm^{-3}, and 3 g cm^{-3} density contours are also plotted for a first look into planet type classification and interior structure.

In the lower plot, we show the planetary mass and orbital period of GEMS and FGK giant planets, colored by planetary equilibrium temperature. The majority of transiting GEMS have an orbital period below 4.5 days. However, GEMS are cooler than FGK hot Jupiters (see color scale of the lower plot, with a maximum of 1000 K) due to the cooler and less massive M dwarf hosts. Therefore, they are unlikely to be inflated due to ohmic dissipation caused by high stellar insolation (D. P. Thorngren & J. J. Fortney 2018).

Among the ∼25 confirmed transiting GEMS so far, this is the tenth whose star has a bound stellar companion (see A. Jordán et al. 2022 for HATS-74Ab, C. I. Cañas et al. 2023 for TOI-3984Ab and TOI-5293Ab, C. I. Cañas et al. 2022 for TOI-3714b, J. D. Hartman et al. 2024 for TOI-762 Ab, and V. Reji et al. 2024, in preparation, for TOI-5688Ab). Details on these planets and their host stars are reported in Table 5. The distribution of the M dwarf binary system projected separation peaks at ∼20–40 au (see J. G. Winters et al. 2019; N. Susemiehl & M. R. Meyer 2022), but no GEMS are found in systems with such tight systems. This could imply that close binary companions might disrupt planet formation processes, while wider separations ($\gtrsim$200 au) are more favorable for the development of giant planets around M dwarfs.

All discovered GEMS can be seen in Figure 6, as well as in Figure 7. Here GEMS and exoplanets around FGK stars are plotted showing the stellar mass versus the planetary-to-stellar mass ratio, colored by planetary equilibrium temperature. GEMS discovered and published by our Survey are highlighted with a black circle.

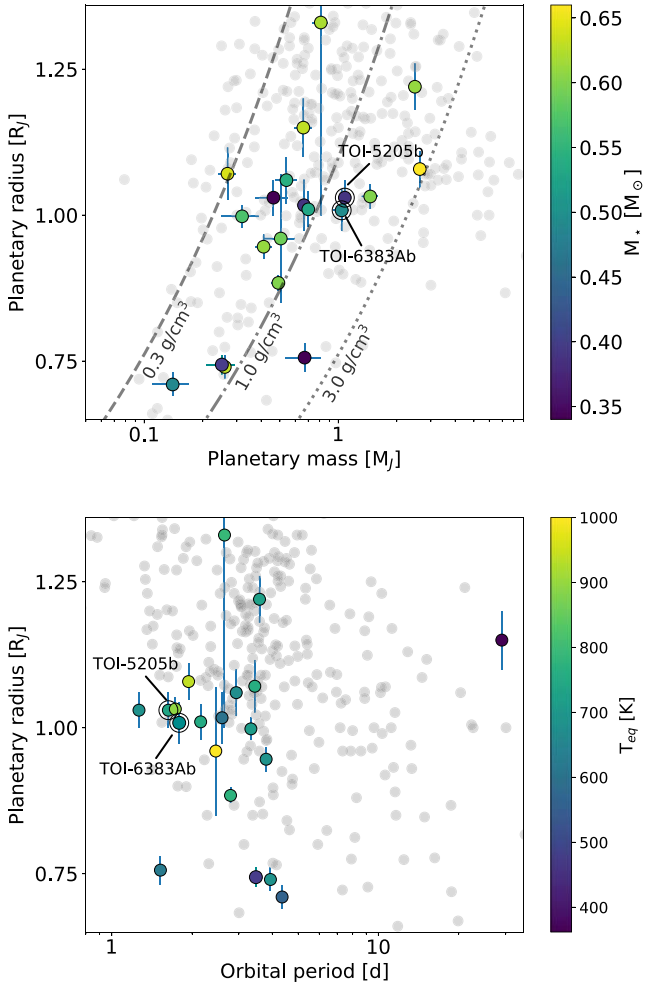

Figure 6. Top plot: mass–radius plane of all known transiting GEMS (colored in the foreground, with error bars) and known planets around F, G, and K stars (in transparency in the background), with planets colored by host star mass. TOI-6383Ab and the similar TOI-5205 b are circled. We also plot the density contours for 0.3 g cm^{-3}, 1 g cm^{-3}, and 3 g cm^{-3}. NGTS-1 b has an imprecise estimate of the radius (the large error bar is clearly visible in the top part of the plot) to due its grazing transit. Bottom plot: orbital period vs. planet radius, colored by planetary equilibrium temperature. TOI-1899b is highlighted because of its long orbital period (∼29 days) with respect to the other GEMS.

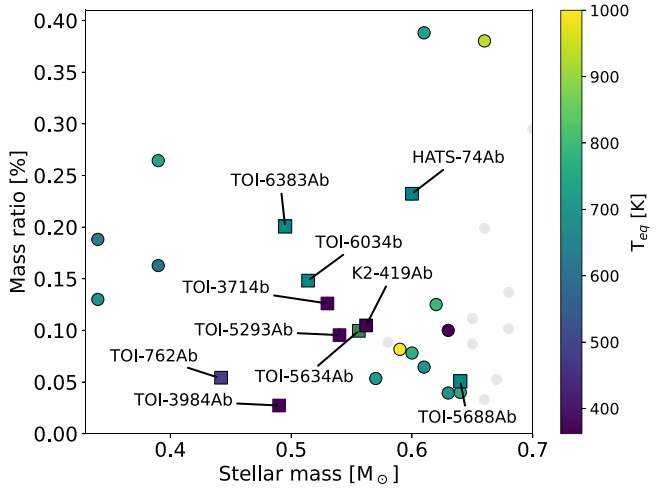

Figure 7. Transiting GEMS (colored) and FGK (in gray) stellar mass vs. the planet-to-star mass ratio, colored by planetary equilibrium temperature. GEMS discovered by the Searching for GEMS survey are circled in black. GEMS in a stellar binary system are represented with a squared marker and labeled with their name. TOI-4201b and HATS-76b correspond to the two higher-mass ratios in the plot, clearly visible on the top right.

The typical large planet-to-star mass ratio (∼0.2%) of such systems may imply strong tidal interactions between the two bodies, in the case of short orbital periods (see, for example, the equations for tidal interactions in Z. Kopal 1978). This could open a new door to the study of gravitational interactions and their consequences on the planetary shape and changes of the orbital elements. Moreover, J. J. Zanazzi et al. (2024) showed that in the case of cool stars ($T_{\rm eff} \lesssim$ 6100 K, with radiative cores) resonance locking can significantly damp the stellar obliquity, orbital semimajor axis, and eccentricity, explaining why cooler stars tend to have spin axes aligned with their hot Jupiters, unlike hotter stars, which lack radiative cores and therefore do not experience the same degree of tidal evolution. In the case of an early M dwarf such as TOI-6383A, the obliquity can be damped even slower due to the very large convective envelope. This makes GEMS interesting targets for Rossiter–McLaughlin measurements to test tidal theories.

Due to their scaled distance to the star (typically, $a/R_\star \gtrsim 10$), these objects may not be tidally locked or circularized like hot Jupiters yet. According to P. Goldreich & S. Soter (1966), Equation (3) of B. Jackson et al. (2008), W. C. Waalkes et al. (2021), and C. M. Persson et al. (2019), the circularization timescale for TOI-6383Ab is 10^9–10^{10} yr depending on the model and assuming Jupiter's tidal quality factor $Q = 10^5$ for the planet, and the tidal decay timescale is 10^{11}–10^{12} yr. This suggests that tidal interactions on these planets are minimal and likely insufficient to cause complete circularization within the star's lifetime. Consequently, the interior and atmospheric properties of GEMS may differ significantly from those of hot Jupiters, which experience more intense tidal interactions. In conclusion, despite the limited number of confirmed GEMS, we can already hypothesize that their interior, atmospheric, and orbital characteristics might not be as similar to hot Jupiters as they might seem at first glance.

5.2. TOI-6383Ab's Interior

We provide a simple calculation of the heavy-element content on the planet. From the relation provided by D. P. Thorngren et al. (2016; fit of their Figure 7), the mass of heavy elements results in ∼59 $M_\oplus$, with a scatter of about 10 $M_\oplus$ due to the scatter of the fit and the uncertainty in the planetary mass. We note that some caveats of such a relation must be considered. The intrinsic spread in the data suggests variability that may not be fully captured by the model, potentially influenced by factors such as the planet's migration history and stochastic nature of formation. Additionally, observational uncertainties and the simplifications in the model, such as not accounting for atmospheric effects or composition gradients, may contribute to the observed scatter in heavy-element mass estimates. Assuming runaway gas accretion onto a ∼10 $M_\oplus$ core, the remaining ∼50 $M_\oplus$ of heavy elements are likely to be spread out through the H/He envelope, similarly to TOI-5205 b (S. Kanodia et al. 2023).

We utilized the planetary evolution model implemented in the `Python` package `planetsynth`, developed by S. Müller & R. Helled (2021). This model is designed to simulate the thermal and structural evolution of giant planets by solving the 1D hydrostatic equilibrium equations (R. Kippenhahn et al. 2013). Key inputs for the model include planetary mass, overall composition (including atmospheric metallicity), and the

Table 5
Details on Host Star, Its Stellar Companion, and the Hosted Planet for the Ten GEMS Hosted by a Binary System

Planet Name	Star Mass A ($M_\odot$)	Star Mass B ($M_\odot$)	Projected Distance (au)	Planet Mass (M_J)	Reference
HATS-74Ab	0.6010 ± 0.0080	0.2284 ± 0.0078	238	1.46 ± 0.14	A. Jordán et al. (2022)
TOI-3714b[a]	0.53 ± 0.02	...	302	0.70 ± 0.03	C. I. Cañas et al. (2022)
TOI-3984Ab[a]	0.49 ± 0.02	...	356	0.14 ± 0.03	C. I. Cañas et al. (2023)
TOI-5293Ab	0.54 ± 0.02	...	579	0.54 ± 0.07	C. I. Cañas et al. (2023)
TOI-762Ab	0.442 ± 0.025	0.227 ± 0.010	319	0.251 ± 0.042	J. D. Hartman et al. (2024)
TOI-5634Ab	0.556 ± 0.022	...	1230	$0.58^{+0.41}_{-0.35}$[c]	S. Kanodia et al. (2024b)
K2-419Ab	0.562 ± 0.024	...	520	0.617 ± 0.047	S. Kanodia et al. (2024b)
TOI-6034b[b]	$0.514^{+0.025}_{-0.022}$	...	4700	0.798 ± 0.075	S. Kanodia et al. (2024b)
TOI-5688Ab	0.64 ± 0.06	0.29 ± 0.06	1100	0.34 ± 0.15	Reji et al., submitted
TOI-6383Ab	0.458 ± 0.011	$0.187^{+0.011}_{-0.013}$	3126	1.040 ± 0.094	This work

Notes.
[a] The stellar companion is a resolved white dwarf. Their stellar mass is not reported in this Table because, as mentioned in the corresponding paper, it was calculated using models, while ideally it should be estimated using low-resolution optical spectra.
[b] TOI-6034b is the first GEMS host which is part of a wide-separation binary with a main sequence companion (late-F star).
[c] A mass upper limit is given in the corresponding paper.

intensity of stellar radiation. The model assumes that giant planets form via the CA process and initially cool adiabatically within a "hot start" scenario (M. S. Marley et al. 2007), characterized by a large initial radius. The evolution of the planet is then tracked over time, providing predictions for changes in planetary radius, luminosity, effective temperature, and surface gravity.

A core–envelope structure is assumed, where the majority of heavy elements are concentrated in a central, compact core. It also takes the effects of stellar irradiation on the planetary atmosphere into account, along with the enrichment of heavy elements in the atmospheric opacity (A. Burrows et al. 2007; S. Müller et al. 2020).

For TOI-6383Ab, we computed the evolutionary track of the planet's radius by fixing the planetary mass and the incident stellar irradiation based on values derived from a joint fit (see Table 4). We then varied the bulk metallicity and atmospheric content of metals to explore their impact on the cooling process. In the top plot of Figure 8, we show the effect of varying the core mass from 7.5 to 50 $M\oplus$ while keeping the atmospheric metallicity $Z_{\rm atm}$ fixed at the solar value of 0.01. According to such a plot, the concentration of heavy elements in the core is below $\sim$40 $M_\oplus$, and more likely $\sim$7.5–30 $M_\oplus$, which aligns with the prediction made by D. P. Thorngren et al. (2016)'s results. Due to the uncertainty in the stellar metallicity, we also recalculated the evolutionary track with $Z_{\rm atm}$ fixed at higher values to account for the fact that TOI-6383A seems to be a moderately metal-rich star. However, the result does not change.

Despite the robustness of the `planetsynth` model, several caveats must be acknowledged. First, the assumption of a "hot start" scenario introduces uncertainty, as the initial conditions of giant planets can vary significantly, particularly if non-adiabatic processes are involved. The assumption of adiabatic cooling may not be valid for all planets, especially those with internal mixing or large composition gradients (A. Vazan et al. 2013, 2015). Additionally, the model does not account for clouds or grains in the atmosphere, which could impact cooling rates by trapping heat (A. Vazan et al. 2013; A. J. Poser et al. 2019). The simplified treatment of stellar irradiation may also lead to inaccuracies, particularly for not extremely irradiated planets (F. Valsecchi et al. 2015). Finally, the assumption of a core–envelope structure without considering composition gradients or more complex internal structures, such as extended, dilute cores (see, e.g., M. Lozovsky et al. 2017) could limit the accuracy of the model predictions.

Comparing the result from such a model with the fitted value of the planetary radius (see Table 4 and the gray-shaded region in the top plot of the figure, assuming the system is not younger than 1 Gyr), we can conclude that the planetary radius is not inflated, as expected from its equilibrium temperature. In the bottom plot, we fixed the mass of the core at 20 $M_\oplus$ and varied the atmospheric metallicity from 1 to 20 $M_\oplus$ (or equivalently from 0.3% to 6%). No value is particularly preferred in this case since all curves agree with our estimated planetary radius.

However, given the assumptions and uncertainties inherent in the actual interior structure models, particularly when only some planetary parameters—e.g., mass, radius, and stellar irradiation—are known, our aim is not to draw definitive conclusions but rather to assess the plausibility of different interior compositions within the context of our observational constraints.

5.3. TOI-6383Ab's Formation

In this section, we will consider both actual giant planet formation scenarios—CA and GI—to assess if one is preferred over the other for TOI-6383Ab. S. Kanodia et al. (2024a) widely discussed the challenges of forming GEMS. First of all, there may not be enough dust mass in protoplanetary disks to support the formation of GEMS during the protoplanetary phase via CA. As a matter of fact, due to the low mass of M dwarfs—ranging from $\sim$0.08$M_\odot$ to $\sim$0.65$M_\odot$—the median Class II disk around such a star is also expected to have a lower median mass compared to solar-type stars (S. M. Andrews et al. 2013; I. Pascucci et al. 2016). The second issue that should be pointed out is the formation timescale of a solid core massive enough to initiate the runaway gaseous accretion phase (G. Laughlin et al. 2004; S. Ida & D. N. C. Lin 2005). At the same orbital distance, the Keplerian orbital timescale is longer for bodies orbiting M dwarfs with respect to FGK stars. Forming a 10 $M_\oplus$ core around an M dwarf star before the disk dissipates is a challenge (see G. Laughlin et al. 2004 and reference therein).

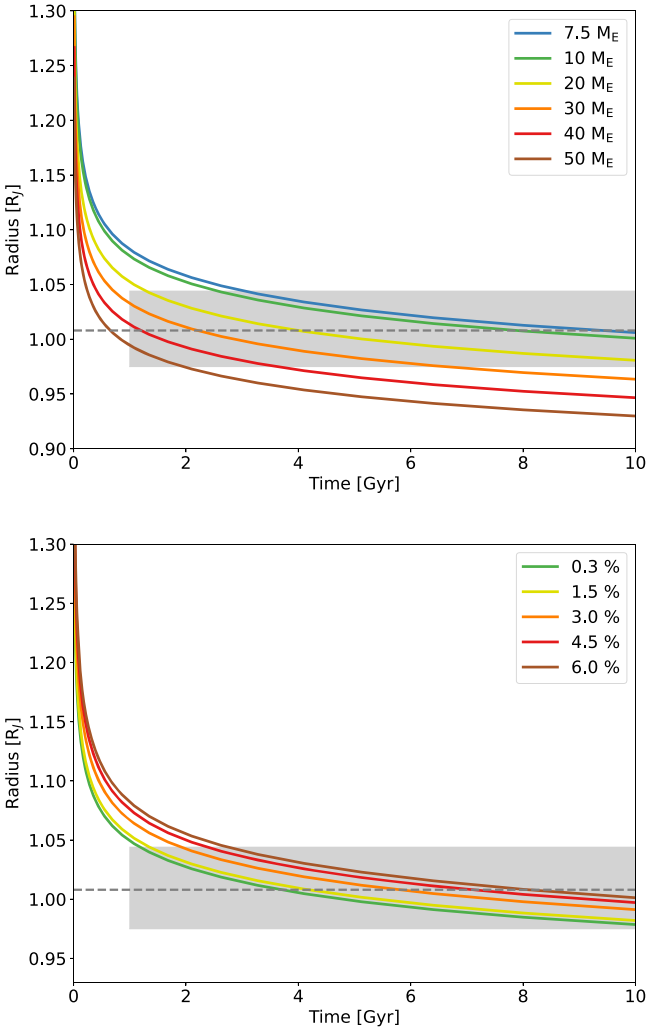

Figure 8. Radius evolution in time of a planet with the mass of TOI-6383Ab, according to the model of S. Müller & R. Helled (2021). Top plot: evolution track of the planetary radius varying its heavy-element (core) mass, and keeping the atmospheric metallicity fixed at the TOI-6383A value. The horizontal dashed line indicates the measured radius of the planet. The gray region corresponds to the 16th and 84th quantiles on the planetary radius, while for the age we only have an indication that the star is not young (>1 Gyr). Colors indicate the core mass, which ranges between 7.5 and 50 M_E. Bottom plot: evolution track of the planetary radius varying the planetary atmospheric metallicity from 0.3% to a maximum of 6% as indicated by the colors (with a fixed core heavy-element mass of 20 $M_\oplus$).

To address the possibility that TOI-8383Ab formed via CA, we make a simple estimate of the mass budget available in the protoplanetary disk to form the planet via core accretion can be done with some assumptions. First, it is reasonable to assume that the disk—and therefore the mass that it contains—should not be truncated by the companion star through gravitational interaction due to the high physical distance between the two stars, unless in the presence of a highly eccentric planetary orbit. The typical size of a protoplanetary disk is a few tens of au in the submillimeter/millimeter dust up to a few hundred for the extension of the gas disks (S. A. Barenfeld et al. 2017; M. Tazzari et al. 2017; M. Ansdell et al. 2018), while the projected distance between the two stars is ∼3100 au (see Table 3).

We can assume the disk-to-star mass ratio between 0.2 and 0.6% (S. M. Andrews et al. 2013, in the Taurus forming region). This implies that the total mass of the protoplanetary disk of TOI-6383A was between ∼300 and 900 $M_\oplus$, respectively when assuming 0.2 and 0.6% for the disk-to-star mass ratio. With a canonical gas-to-dust mass content ratio of the interstellar medium of 100:1, the dust mass ranges between ∼3 and 9 $M_\oplus$. Even supposing that the entire available mass converged to form TOI-6383Ab, this quantity would be insufficient to form a core of 10 $M_\oplus$ in the core accretion formation scenario, necessary to initiate runaway gaseous accretion. Moreover, the content of dust available is definitely lower than the predicted mass from Section 5.2, of 7.5–30 $M_\oplus$ in the core and an additional few $M_\oplus$ in the atmosphere.

Even in the most massive disk (i.e., almost gravitationally unstable, ∼150–200 $M_\oplus$), a planet of ∼60 $M_\oplus$ of heavy elements (contained partly in the core and partly in the atmosphere, as calculated in Section 5.2) would require a formation efficiency of ∼30%–40% to form via core accretion, in contrast with the nominal value of 10% (J. W. Lin et al. 2018) from formation models of pebble accretion.

However, there is some scatter in these scaling relations. We could hypothesize that the disk around TOI-6383A was more massive than predicted. S. M. Andrews et al. (2013) pointed out some outliers within their sample of Taurus disks, noting their unusually high masses, whose disk-to-stellar mass ratio is around 10%. If that is the case, there could have been enough material to form the core and then subsequently the planet. On the other hand, with different assumptions on the gas-to-dust ratio (e.g., ∼70:1 for the solar medium, R. C. Bohlin et al. 1978), the total mass content can vary between ∼4 and ∼13 $M_\oplus$ (calculated assuming 0.2 and 0.6% for the disk-to-star mass ratio, respectively).

We also want to highlight a few caveats in this discussion. First of all, the dust mass measured by the Atacama Large Millimeter/submillimeter Array (ALMA) in millimeter-sized particles does not accurately reflect the original mass budget. The formation process has already begun; therefore part of the dust is already aggregated in larger particles than the observed millimeter-sized ones (J. S. Greaves & W. K. M. Rice 2010; J. R. Najita & S. J. Kenyon 2014). Moreover, due to interactions with the gas present in the disk and the effect of radiation pressure, dust particles tend to migrate radially inward in the disk, eventually falling onto the central star. This phenomenon also causes dust depletion (J. Appelgren et al. 2023). Furthermore, the dust mass in protoplanetary disks is typically estimated based on continuum flux measurement of millimeter-sized dust particles by assuming blackbody emission and with a single wavelength, at 850 μm (R. H. Hildebrand 1983). The straightforward relation between flux and dust mass is valid if there are no structures in the disk—such as rings or gaps, Y. Liu et al. (2022)—and if the continuum emission is optically thin (R. H. Hildebrand 1983). If one of these conditions is not met, the amount of dust can be underestimated by a factor between 3 and 10 (Y. Liu et al. 2022).

It is worth mentioning that recent numerical simulations by S. Savvidou & B. Bitsch (2024) of planet formation via pebble and gas accretion in a viscously evolving protoplanetary disk, suggest that, especially if the planet forms in the inner disk, hidden dust mass, coupled with early planet formation, might address the hypothetical mass budget problem.

Given the limitations of existing dust mass measurements from ALMA in accessing the primordial mass budget available for formation via CA. Miotello et al. (2023), we instead consider the most massive disks possible before the onset of GI

(A. P. Boss 2006, 2011; A. P. Boss & S. Kanodia 2023). GI becomes possible for disks that are ∼10%–15% of the host star mass for ∼0.46 $M_{\odot}$ stars (Figure 7 in A. P. Boss & S. Kanodia 2023). Assuming this to be the maximum disk mass for CA, and the standard gas-to-dust mass ratio of 100:1, this corresponds to a minimum dust mass content of ∼150–200 $M_{\oplus}$. A compilation of ALMA observations (Figure 6 of C. F. Manara et al. 2023) also shows that the most massive disk around an M dwarf has ∼140 $M_{\oplus}$ of dust mass, below the minimum amount required to initiate GI.

In summary, while the CA scenario could explain the formation of TOI-6383Ab under the assumption of an unusually massive dust-rich disk and a higher-than-average core formation efficiency, this scenario still faces significant challenges. It also entails the core formation efficiency for GEMS to be much higher than 10%, or if we assume that the core formation efficiency is still 10%, then these GEMS accrete a significant heavy-element fraction through post-formation processes such as late-stage pollution (S.-F. Liu et al. 2015). Besides the high demand for dust mass in the disk and a high formation efficiency, another challenge in CA is the pebble isolation mass (B. Liu et al. 2019). The conclusion of the pebble accretion phase is significantly influenced by the stellar mass and defines the characteristic mass of planets, as it effectively stops further growth through pebble accretion.

Alternatively, GI is shown to be a plausible alternative by recent studies (see, e.g., A. P. Boss & S. Kanodia 2023), especially given the possibility of forming the planet in a marginally stable disk. However, in the case of TOI-6383A, GI would require a minimum dust mass greater than any observed in disks around M dwarfs.

Currently, neither scenario can be definitively identified as the formation path for TOI-6383Ab. The conventional mechanisms for gas giant formation are especially challenging when applied to GEMS, indicating that these are likely rare objects, regardless of whether they formed through CA or GI, in agreement with transiting occurrence rate studies from T. Gan et al. (2023) and E. M. Bryant et al. (2023). A larger sample of transiting GEMS with well-characterized planetary properties and stellar metallicities (despite the complexities in its determination in the case of M dwarf) could help distinguish between the two, as is the goal of our search for the GEMS survey (S. Kanodia et al. 2024a).

6. Conclusions

We report the discovery of TOI-6383Ab, a massive Jovian planet around a nearby M star as part of the Search for Giant Exoplanets around M dwarf Stars survey. TOI-6383Ab has a radius of $1.008\ ^{+0.036}_{-0.033}\ R_J$, a mass of $1.040 \pm 0.094\ M_J$, and a density of $1.26\ ^{+0.18}_{-0.17}$ g cm^{-3} around the early-type M dwarf star TOI-6383A. The target was identified in TESS data, and then ground-based transit and radial velocity observations followed to confirm and characterize it.

We also detected a 0.2 $M_{\odot}$ M dwarf stellar companion of TOI-6383A. The discovery of TOI-6383Ab marks the tenth instance among ∼25 confirmed transiting GEMS where the host star has a bound stellar companion.

As discussed, the formation of GEMS presents significant challenges, particularly when considering the conventional mechanisms of gas giant formation, CA and GI. Both scenarios require specific and often rare conditions, such as unusually massive and dust-rich protoplanetary disks, to successfully form GEMS. The formation of TOI-6383Ab still remains an open question. It likely formed in an exceptionally massive, dust-rich disk, with a core formation efficiency exceeding the nominal 10% value, and notably, boasting a high planet-to-stellar mass ratio of ∼0.2%. Alternatively, GI offers a viable explanation, given a massive enough protoplanetary disk.

Delineating and differentiating the properties of GEMS, such as their mass, orbital characteristics, and atmospheric compositions, is essential for constraining theoretical models and refining our understanding of planetary formation processes. Moreover, it is worth pointing out that due to the low stellar-to-planet-mass ratio, GEMS is a favorable target when it comes to investigating the tidal decay of the planetary orbit.

Acknowledgments

This work was supported by the European Union's Horizon Europe Framework Programme under Marie Skłodowska-Curie Actions grant agreement No. 101086149 (EXOWORLD).

The work was also supported by DFG Research Unit 2440: "Matter Under Planetary Interior Conditions: High Pressure, Planetary, and Plasma Physics."

C.I.C. acknowledges support by NASA Headquarters through an appointment to the NASA Postdoctoral Program at the Goddard Space Flight Center, administered by ORAU through a contract with NASA.

This work is based on observations obtained with the Hobby–Eberly Telescope (HET), which is a joint project of the University of Texas at Austin, the Pennsylvania State University, Ludwig-Maximillians-Universitaet Muenchen, and Georg-August Universitaet Goettingen. HET is named in honor of its principal benefactors, William P. Hobby and Robert E. Eberly.

These results are based on observations obtained with the Habitable-zone Planet Finder Spectrograph on HET. The HPF team acknowledges support from NSF grants AST-1006676, AST-1126413, AST-1310885, AST-1517592, AST-1310875, ATI-2009889, ATI-2009982, AST-2108512, AST-2108801, and the NASA Astrobiology Institute (NNA09DA76A) in the pursuit of precision radial velocities in the NIR. The HPF team also acknowledges support from the Heising-Simons Foundation via grant 2017-0494.

The HET collaboration acknowledges the support and resources from the Texas Advanced Computing Center. We thank the Resident astronomers and Telescope Operators at the HET for the skillful execution of our observations with HPF. We would like to acknowledge that the HET is built on Indigenous land. Moreover, we would like to acknowledge and pay our respects to the Carrizo and Comecrudo, Coahuiltecan, Caddo, Tonkawa, Comanche, Lipan Apache, Alabama-Coushatta, Kickapoo, Tigua Pueblo, and all the American Indian and Indigenous Peoples and communities who have been or have become a part of these lands and territories in Texas, here on Turtle Island.

We acknowledge the Texas Advanced Computing Center (TACC) at The University of Texas at Austin for providing high-performance computing, visualization, and storage resources that have contributed to the results reported within this paper.

The Low-resolution Spectrograph 2 (LRS-2) was developed and funded by the University of Texas at Austin McDonald Observatory and Department of Astronomy and by Pennsylvania State University. We thank the Leibniz-Institut fuer

Astrophysik Potsdam (AIP) and the Institut fuer Astrophysik Goeottingen (IAG) for their contributions to the construction of the integral field units.

Some of the observations in this paper made use of the NN-EXPLORE Exoplanet and Stellar Speckle Imager (NESSI). NESSI was funded by the NASA Exoplanet Exploration Program and the NASA Ames Research Center. NESSI was built at the Ames Research Center by Steve B. Howell, Nic Scott, Elliott P. Horch, and Emmett Quigley. The observations fall under the program number 2023B-438370 (PI: Kanodia).

This research has made use of the Exoplanet Follow-up Observation Program (ExoFOP; DOI: 10.26134/ExoFOP5) website, which is operated by the California Institute of Technology, under contract with the National Aeronautics and Space Administration under the Exoplanet Exploration Program.

We extend our sincere appreciation to the staff of the RBO telescope facility whose expertize was vital in the success of this research paper.

This research has made use of the NASA Exoplanet Archive, which is operated by the California Institute of Technology, under contract with the National Aeronautics and Space Administration under the Exoplanet Exploration Program.

This work has made use of data from the European Space Agency (ESA) mission Gaia,[28] processed by the Gaia Data Processing and Analysis Consortium (DPAC[29]). Funding for the DPAC has been provided by national institutions, in particular, the institutions participating in the Gaia Multilateral Agreement.

This publication makes use of data products from the Two Micron All Sky Survey (2MASS), which is a joint project of the University of Massachusetts and the Infrared Processing and Analysis Center/California Institute of Technology, funded by the National Aeronautics and Space Administration and the National Science Foundation.

This publication makes use of data products from the Wide-field Infrared Survey Explorer, which is a joint project of the University of California, Los Angeles, and the Jet Propulsion Laboratory/California Institute of Technology, and NEOWISE, which is a project of the Jet Propulsion Laboratory/California Institute of Technology. WISE and NEOWISE are funded by the National Aeronautics and Space Administration.

This research was made possible through the use of the AAVSO Photometric All-Sky Survey (APASS), funded by the Robert Martin Ayers Sciences Fund and NSF AST-1412587.

Facilities: TESS, HET (HPF), RBO, Gaia, Nasa Exoplanet Archive, 2MASS, APASS, WISE, LRS-2, NESSI, ZTF, ASAS-SN. All the TESS data used in this paper can be found in MAST:10.17909/h9vj-t740.

ORCID iDs

Lia Marta Bernabò https://orcid.org/0000-0002-8035-1032
Shubham Kanodia https://orcid.org/0000-0001-8401-4300
Caleb I. Cañas https://orcid.org/0000-0003-4835-0619
William D. Cochran https://orcid.org/0000-0001-9662-3496
Szilárd Csizmadia https://orcid.org/0000-0001-6803-9698
Suvrath Mahadevan https://orcid.org/0000-0001-9596-7983
Gudhmundur Stefánsson https://orcid.org/0000-0001-7409-5688
Arvind F. Gupta https://orcid.org/0000-0002-5463-9980
Andrew Monson https://orcid.org/0000-0002-0048-2586
Henry A. Kobulnicky https://orcid.org/0000-0002-4475-4176
Alexander K. Larsen https://orcid.org/0000-0002-2401-8411
Ethan G. Cotter https://orcid.org/0009-0003-1637-8315
Tera N. Swaby https://orcid.org/0000-0002-5817-202X
Gregory Zeimann https://orcid.org/0000-0003-2307-0629
Chad F. Bender https://orcid.org/0000-0003-4384-7220
Scott A. Diddams https://orcid.org/0000-0002-2144-0764
Jessica E. Libby-Roberts https://orcid.org/0000-0002-2990-7613
Andrea S. J. Lin https://orcid.org/0000-0002-9082-6337
Joe P. Ninan https://orcid.org/0000-0001-8720-5612
Heike Rauer https://orcid.org/0000-0002-6510-1828
Varghese Reji https://orcid.org/0009-0006-7298-619X
Paul Robertson https://orcid.org/0000-0003-0149-9678
Arpita Roy https://orcid.org/0000-0001-8127-5775
Christian Schwab https://orcid.org/0000-0002-4046-987X

[28] https://www.cosmos.esa.int/gaia
[29] https://www.cosmos.esa.int/web/gaia/dpac/consortium

References

Akeson, R. L., Chen, X., Ciardi, D., et al. 2013, PASP, 125, 989
Andrews, S. M., Rosenfeld, K. A., Kraus, A. L., & Wilner, D. J. 2013, ApJ, 771, 129
Anglada-Escudé, G., & Butler, R. P. 2012, ApJS, 200, 15
Ansdell, M., Williams, J. P., Trapman, L., et al. 2018, ApJ, 859, 21
Appelgren, J., Lambrechts, M., & van der Marel, N. 2023, A&A, 673, A139
Astropy Collaboration, Robitaille, T. P., Tollerud, E. J., et al. 2013, A&A, 558, A33
Barenfeld, S. A., Carpenter, J. M., Sargent, A. I., Isella, A., & Ricci, L. 2017, ApJ, 851, 85
Bellm, E. C., Kulkarni, S. R., Graham, M. J., et al. 2019, PASP, 131, 018002
Bensby, T., Feltzing, S., & Oey, M. S. 2014, A&A, 562, A71
Bessell, M. S. 1990, PASP, 102, 1181
Bohlin, R. C., Savage, B. D., & Drake, J. F. 1978, ApJ, 224, 132
Boss, A. P. 1997, Sci, 276, 1836
Boss, A. P. 2006, ApJ, 643, 501
Boss, A. P. 2011, ApJ, 731, 74
Boss, A. P., & Kanodia, S. 2023, ApJ, 956, 4
Bovy, J. 2015, ApJS, 216, 29
Bradley, L., Sipőcz, B., Robitaille, T., et al. 2023, astropy/photutils: v1.8.0, Zenodo, doi:10.5281/zenodo.7946442
Bryant, E. M., Bayliss, D., & Van Eylen, V. 2023, MNRAS, 521, 3663
Burn, R., Schlecker, M., Mordasini, C., et al. 2021, A&A, 656, A72
Burrows, A., Hubeny, I., Budaj, J., & Hubbard, W. B. 2007, ApJ, 661, 502
Cañas, C. I., Kanodia, S., Bender, C. F., et al. 2022, AJ, 164, 50
Cañas, C. I., Kanodia, S., Libby-Roberts, J., et al. 2023, AJ, 166, 30
Carter, J. A., & Winn, J. N. 2009, ApJ, 704, 51
Chonis, T. S., Hill, G. J., Lee, H., et al. 2016, Proc. SPIE, 9908, 99084C
Clough, S. A., Shephard, M. W., Mlawer, E. J., et al. 2005, JQSRT, 91, 233
Covey, K. R., Ivezić, Ž., Schlegel, D., et al. 2007, AJ, 134, 2398
Csizmadia, S. 2020, MNRAS, 496, 4442
Csizmadia, S., Smith, A. M. S., Kálmán, S., et al. 2023, A&A, 675, A106
Duque-Arribas, C., Montes, D., Tabernero, H. M., et al. 2023, ApJ, 944, 106
Eastman, J., 2012 Time Utilities, Astrophysics Source Code Library, ascl:1206.012
El-Badry, K., & Rix, H.-W. 2018, MNRAS, 480, 4884
Feinstein, A. D., Montet, B. T., Foreman-Mackey, D., et al. 2019, PASP, 131, 094502
Ford, E. B. 2006, ApJ, 642, 505
Foreman-Mackey, D., Luger, R., Agol, E., et al. 2021, exoplanet: Gradient-based Probabilistic Inference for Exoplanet Data & Other Astronomical Time Series, v0.5.1, Zenodo, doi:10.5281/zenodo.7191939
Gaia Collaboration, Brown, A. G. A., Vallenari, A., et al. 2018, A&A, 616, A1
Gaia Collaboration, Prusti, T., de Bruijne, J. H. J., et al. 2016, A&A, 595, A1
Gaia Collaboration, Vallenari, A., Brown, A. G. A., et al. 2023, A&A, 674, A1
Gan, T., Wang, S. X., Wang, S., et al. 2023, AJ, 165, 17

Gelman, A., & Rubin, D. B. 1992, StaSc, 7, 457
Goldreich, P., & Soter, S. 1966, Icar, 5, 375
Graham, M. J., Kulkarni, S. R., Bellm, E. C., et al. 2019, PASP, 131, 078001
Greaves, J. S., & Rice, W. K. M. 2010, MNRAS, 407, 1981
Gullikson, K., Dodson-Robinson, S., & Kraus, A. 2014, AJ, 148, 53
Hartman, J. D., Bayliss, D., Brahm, R., et al. 2024, AJ, 168, 202
Henden, A. A., Levine, S., Terrell, D., et al. 2018, AAS Meeting Abstracts, 232, 223.06
Hildebrand, R. H. 1983, QJRAS, 24, 267
Hill, G. J., Lee, H., MacQueen, P. J., et al. 2021, AJ, 162, 298
Hogg, D. W., Blanton, M., Lang, D., Mierle, K., & Roweis, S. 2008, in ASP Conf. Ser. 394, Astronomical Data Analysis Software and Systems XVII, ed. R. W. Argyle, P. S. Bunclark, & J. R. Lewis (San Francisco, CA: ASP), 27
Howell, S. B., Everett, M. E., Sherry, W., Horch, E., & Ciardi, D. R. 2011, AJ, 142, 19
Ida, S., & Lin, D. N. C. 2005, ApJ, 626, 1045
Jackson, B., Greenberg, R., & Barnes, R. 2008, ApJ, 678, 1396
Jayasinghe, T., Stanek, K. Z., Kochanek, C. S., et al. 2019, MNRAS, 485, 961
Jordán, A., Hartman, J. D., Bayliss, D., et al. 2022, AJ, 163, 125
Kanodia, S., Cañas, C. I., Mahadevan, S., et al. 2024a, AJ, 167, 161
Kanodia, S., Gupta, A. F., Cañas, C. I., et al. 2024b, AJ, 168, 235
Kanodia, S., Libby-Roberts, J., Cañas, C. I., et al. 2022, AJ, 164, 81
Kanodia, S., Mahadevan, S., Libby-Roberts, J., et al. 2023, AJ, 165, 120
Kanodia, S., Mahadevan, S., Ramsey, L. W., et al. 2018, Proc. SPIE, 10702, 107026Q
Kanodia, S., & Wright, J. 2018, RNAAS, 2, 4
Kasper, D. H., Ellis, T. G., Yeigh, R. R., et al. 2016, PASP, 128, 105005
Kesseli, A., West, A. A., Harrison, B., Veyette, M., & Feldman, D. 2017, AAS Meeting Abstracts, 229, 240.35
Kiman, R., Schmidt, S. J., Angus, R., et al. 2019, AJ, 157, 231
Kippenhahn, R., Weigert, A., & Weiss, A. 2013, Stellar Structure and Evolution (Berlin: Springer)
Kipping, D. M. 2013, MNRAS, 435, 2152
Kopal, Z. 1978, Dynamics of Close Binary Systems (Berlin: Springer)
Kunimoto, M., Daylan, T., Guerrero, N., et al. 2022, ApJS, 259, 33
Laughlin, G., Bodenheimer, P., & Adams, F. C. 2004, ApJL, 612, L73
Lee, H., Chonis, T. S., Hill, G. J., et al. 2010, Proc. SPIE, 7735, 77357H
Lin, J. W., Lee, E. J., & Chiang, E. 2018, MNRAS, 480, 4338
Liu, B., Lambrechts, M., Johansen, A., & Liu, F. 2019, A&A, 632, A7
Liu, S.-F., Agnor, C. B., Lin, D. N. C., & Li, S.-L. 2015, MNRAS, 446, 1685
Liu, Y., Linz, H., Fang, M., et al. 2022, A&A, 668, A175
Lozovsky, M., Helled, R., Rosenberg, E. D., & Bodenheimer, P. 2017, ApJ, 836, 227
Mahadevan, S., Anderson, T., Balderrama, E., et al. 2018, Proc. SPIE, 10702, 1070214
Mahadevan, S., Ramsey, L., Bender, C., et al. 2012, Proc. SPIE, 8446, 84461S
Mahadevan, S., Ramsey, L. W., Terrien, R., et al. 2014, Proc. SPIE, 9147, 91471G
Manara, C. F., Ansdell, M., Rosotti, G. P., et al. 2023, in ASP Conf. Ser. 534, Protostars and Planets VII, ed. S. Inutsuka et al. (San Francisco, CA: ASP), 539
Mann, A. W., Feiden, G. A., Gaidos, E., Boyajian, T., & von Braun, K. 2015, ApJ, 804, 64
Marley, M. S., Fortney, J. J., Hubickyj, O., Bodenheimer, P., & Lissauer, J. J. 2007, ApJ, 655, 541
Mercer, A., & Stamatellos, D. 2020, A&A, 633, A116
Metcalf, A. J., Anderson, T., Bender, C. F., et al. 2019, Optic, 6, 233
Miotello, A., Kamp, I., Birnstiel, T., Cleeves, L. C., & Kataoka, A. 2023, in ASP Conf. Ser. 534, Protostars and Planets VII, ed. S. Inutsuka et al. (San Francisco, CA: ASP), 501
Mizuno, H. 1980, PThPh, 64, 544
Müller, S., Ben-Yami, M., & Helled, R. 2020, ApJ, 903, 147
Müller, S., & Helled, R. 2021, MNRAS, 507, 2094
Najita, J. R., & Kenyon, S. J. 2014, MNRAS, 445, 3315
Ninan, J. P., Bender, C. F., Mahadevan, S., et al. 2018, Proc. SPIE, 10709, 107092U
Pascucci, I., Testi, L., Herczeg, G. J., et al. 2016, ApJ, 831, 125
Persson, C. M., Csizmadia, S., Mustill, A. J., et al. 2019, A&A, 628, A64
Pollack, J. B., Hubickyj, O., Bodenheimer, P., et al. 1996, Icar, 124, 62
Poser, A. J., Nettelmann, N., & Redmer, R. 2019, Atmos, 10, 664
Rabus, M., Lachaume, R., Jordan, A., et al. 2019, MNRAS, 484, 2674
Ramsey, L. W., Adams, M. T., Barnes, T. G., et al. 1998, Proc. SPIE, 3352, 34
Ricker, G. R., Winn, J. N., Vanderspek, R., et al. 2015, JATIS, 1, 014003
Roulston, B. R., Green, P. J., & Kesseli, A. Y. 2020, ApJS, 249, 34
Salvatier, J., Wieckiâ, T. V., & Fonnesbeck, C., 2016 PyMC3: Python probabilistic programming framework, Astrophysics Source Code Library, ascl:1610.016
Savvidou, S., & Bitsch, B. 2024, arXiv:2407.08533
Schönrich, R., Binney, J., & Dehnen, W. 2010, MNRAS, 403, 1829
Schweitzer, A., Passegger, V. M., Cifuentes, C., et al. 2019, A&A, 625, A68
Scott, N. J., Howell, S. B., Horch, E. P., & Everett, M. E. 2018, PASP, 130, 054502
Shappee, B., Prieto, J., Stanek, K. Z., et al. 2014, AAS Meeting Abstracts, 223, 236.03
Skrutskie, M. F., Cutri, R. M., Stiening, R., et al. 2006, AJ, 131, 1163
Stefansson, G., Cañas, C., Wisniewski, J., et al. 2020, AJ, 159, 100
Stefansson, G., Hearty, F., Robertson, P., et al. 2016, ApJ, 833, 175
Susemiehl, N., & Meyer, M. R. 2022, A&A, 657, A48
Tazzari, M., Testi, L., Natta, A., et al. 2017, A&A, 606, A88
Thorngren, D. P., & Fortney, J. J. 2018, AJ, 155, 214
Thorngren, D. P., Fortney, J. J., Murray-Clay, R. A., & Lopez, E. D. 2016, ApJ, 831, 64
Tychoniec, Ł., Manara, C. F., Rosotti, G. P., et al. 2020, A&A, 640, A19
Valsecchi, F., Rappaport, S., Rasio, F. A., Marchant, P., & Rogers, L. A. 2015, ApJ, 813, 101
Vazan, A., Helled, R., Kovetz, A., & Podolak, M. 2015, ApJ, 803, 32
Vazan, A., Kovetz, A., Podolak, M., & Helled, R. 2013, MNRAS, 434, 3283
Waalkes, W. C., Berta-Thompson, Z. K., Collins, K. A., et al. 2021, AJ, 161, 13
Winters, J. G., Henry, T. J., Jao, W.-C., et al. 2019, AJ, 157, 216
Wright, E. L., Eisenhardt, P. R. M., Mainzer, A. K., et al. 2010, AJ, 140, 1868
Wright, J. T., & Eastman, J. D. 2014, PASP, 126, 838
Yan, R., Chen, Y., Lazarz, D., et al. 2019, ApJ, 883, 175
Yee, S. W., Petigura, E. A., & von Braun, K. 2017, ApJ, 836, 77
Zanazzi, J. J., Dewberry, J., & Chiang, E. 2024, ApJL, 967, L29
Zechmeister, M., Reiners, A., Amado, P. J., et al. 2018, A&A, 609, A12